文章编号：1001-9014(2025)04-0511-09

DOI:10.11972/j.issn.1001-9014.2025.04.005

Research on variable-speed scanning method for airborne area-array whisk-broom imaging system based on vertical flight path correction

JIN Jia-Rong[1,2], HAN Gui-Cheng[1], WANG Chong-Ru[1,2], WU Ren-Fei[1,2], WANG Yue-Ming[1,2,3*]

(1. Key Laboratory of Space Active Opto-Electronics Technology, Shanghai Institute of Technical Physics, Chinese Academy of Sciences, Shanghai 200083, China;
2. University of Chinese Academy of Sciences, Beijing 100049, China;
3. Hangzhou Institute for Advanced Study, University of Chinese Academy of Sciences, Hangzhou 310024, China)

Abstract: Airborne area-array whisk-broom imaging systems typically adopt constant-speed scanning schemes. For large-inertia scanning systems, constant-speed scanning requires substantial time to complete the reversal motion, reducing the system´s adaptability to high-speed reversal scanning and decreasing scanning efficiency. This study proposes a novel sinusoidal variable-speed roll scanning strategy, which reduces abrupt changes in speed and acceleration, minimizing time loss during reversals. Based on the forward image motion compensation strategy in the pitch direction, we establish a line-of-sight (LOS) position calculation model with vertical flight path correction (VFPC), ensuring that the central LOS of the scanned image remains stable on the same horizontal line, facilitating accurate image stitching in whisk-broom imaging. Through theoretical analysis and simulation experiments, the proposed method improves the scanning efficiency by approximately 18.6% at a 90° whisk-broom imaging angle under the same speed height ratio conditions. The new VFPC method enables wide-field, high-resolution imaging, achieving single-line LOS horizontal stability with an accuracy of better than 0.4 mrad. The research is of great significance to promote the further development of airborne area-array whisk-broom imaging technology toward wider fields of view, higher speed height ratios, and greater scanning efficiency.

Key words: airborne remote sensing, whisk-broom imaging, image motion, vertical flight path correction (VFPC), line-of-sight (LOS) stabilization

基于垂直航迹校正的机载面阵摆扫成像系统变速扫描方法研究

金家融[1,2], 韩贵丞[1], 王崇儒[1,2], 吴任飞[1,2], 王跃明[1,2,3*]

(1. 中国科学院上海技术物理研究所 空间主动光电技术重点实验室,上海 200083;
2. 中国科学院大学, 北京 100049;
3. 国科大杭州高等研究院,浙江 杭州 310024)

摘要:机载面阵摆扫成像系统多采用匀速扫描方案,对于大惯量的整机摆扫系统,匀速式扫描需要消耗大量时间完成换向动作,制约了高速换向扫描时的适应能力,限制了系统的扫描效率。本文提出了一种正弦型的新型变速横滚扫描策略,减小速度与加速度突变,降低换向时间损耗。基于俯仰方向的前向像移补偿策略,建立了垂直航迹校正的视轴位置计算模型,使扫描图像中心视轴稳定在同一水平线,有利于摆扫图像的准确拼接。经理论分析与仿真实验验证,在90°摆扫成像角度,相同速高比条件下,扫描效率可提高约18.6%。采用新的垂直航迹计算方法,实现了宽视场高分辨率成像,单行视轴水平稳定精度优于0.4 mrad。论文研究工作对推动机载面阵摆扫成像技术向着宽视场、大速高比、高扫描效率方向的进一步发展具有重要意义。

关 键 词:航空遥感;摆扫成像;像移;垂直航迹校正;视轴稳定

中图分类号:P237　　**文献标识码**:A

Received date: 2024-10-31, **revised date**: 2025-02-24　　**收稿日期**:2024-10-31, **修回日期**:2025-02-24

Foundation items: Supported by the National Key Research and Development Program (2023YFC3107602)

Biography: JIN Jia-Rong (1998-), male, Shenyang, China, Ph. D. Research areas involve airborne area-array scanning systems, line-of-sight stabilization systems. E-mail: jinjiarong_ucas@163.com

* **Corresponding author**: E-mail: wangym@mail.sitp.ac.cn

Introduction

Airborne infrared electro-optical imaging technology is progressing rapidly toward wide-field and high-resolution imaging [1-3]. Typical scanning methods for area-array detectors include single-pass scanning [2-3] and double-pass whisk-broom scanning [4]. To balance wide-field and high-resolution imaging under the constraints of a limited area-array while improving scanning efficiency to extend effective imaging time, an increasing number of airborne cameras have adopted double-pass constant-speed whisk-broom imaging schemes [5-6]. However, under high speed-to-height ratio conditions, the scanning time per pass is shortened, necessitating an increase in scanning speed, which in turn exacerbates time loss during reversals. Due to the limited peak torque output of the motors, further improving scanning efficiency is a challenge. Therefore, to further extend effective imaging time and enhance system efficiency, optimizing the scanning strategy to minimize time loss during reversals is essential.

Airborne imaging systems primarily rely on Position and Orientation System (POS) data to determine system orientation[7-8], applying compensation based on positional and attitude information [9-10]. Studies on forward image motion compensation during aircraft flight have achieved promising results using constant-speed return-sweep compensation schemes to stabilize the LOS at the aircraft's ground projection point [11-12]. This method is straightforward and effectively enables track-following scanning trajectories under constant-speed whisk-broom scanning in the wingspan direction, meeting the forward overlap requirements of double-pass whisk-broom scanning. However, theoretical calculations indicate that the ground projection of this constant-speed return-sweep compensation trajectory follows a hyperbola path. At large forward-motion angle conditions, long single-frame exposures cause image motion, resulting in blurred images. As whisk-broom imaging technology evolves toward wider fields of view and larger total scan angles, deviations caused during large-tilt-angle scans become more pronounced. Consequently, a new forward image motion compensation scheme is needed to meet the requirements of next-generation airborne cameras for wide-field imaging and high speed-to-height ratios.

To address the limitations of the constant-speed whisk-broom scanning scheme regarding scanning efficiency, as well as the inapplicability of traditional constant-speed return-sweep compensation methods in variable-speed roll scanning, this study proposes a novel sinusoidal variable-speed scanning strategy. This approach develops a LOS position calculation model with VFPC and incorporates forward image motion compensation, focusing on the high-accuracy compensation control curve for the pitch scanning mirror. Through software simulation modeling and hardware verification, the control curve algorithm was optimized to enhance the precision and real-time performance of the compensation, and the effectiveness of the proposed method is validated through simulated flight imaging experiments.

1 Imaging model of area-array camera system

1.1 Imaging principle and system parameters

The schematic structure of the wide-field imaging system with wingspan whisk-broom scanning is shown in Fig. 1. The area-array camera is horizontally fixed on the roll gimbal, achieving high-resolution ground imaging by deflecting of the optical path via a reflective mirror. The pitch mirror rotates around the pitch axis to compensate for field-of-view (FOV) deviations caused by pitch attitude disturbances of the system, ensuring that the LOS during each imaging pass always points to the initial exposure position, thus providing forward motion compensation for target tracking. The roll gimbal rotates around the roll axis to compensate for FOV deviations caused by roll attitude disturbances while performing wide-field imaging in the wingspan direction. An image motion compensation mechanism is integrated into the roll axis to counteract image blurring caused by wingspan scanning motion during exposure.

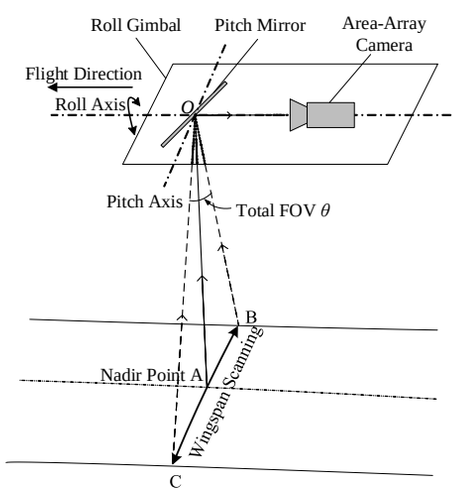

Fig. 1 Imaging structure of the whole machine with wingspan pendulum sweep
图1 整机翼展摆扫宽视场成像结构示意图

In area-array scanning imaging, FOV overlap is required to ensure seamless image stitching. The overlap occurs in both the forward flight direction and the roll wingspan direction, as illustrated in Fig. 2. The aircraft's flight altitude is H, flight speed is v, and the detector has a size of $m \times n$, with an instantaneous field of view (IFOV) angle of β and a total FOV angle of θ.

The FOV overlap ratio is denoted as ρ, and during each scan, the forward flight distance of the aircraft is L, with a scan time of t. Due to time losses during the reversal motion, the scanning efficiency is η, the effective scanning time is t_{eff}, and the scanning angular velocity is ω. The expressions for these parameters are as fol-

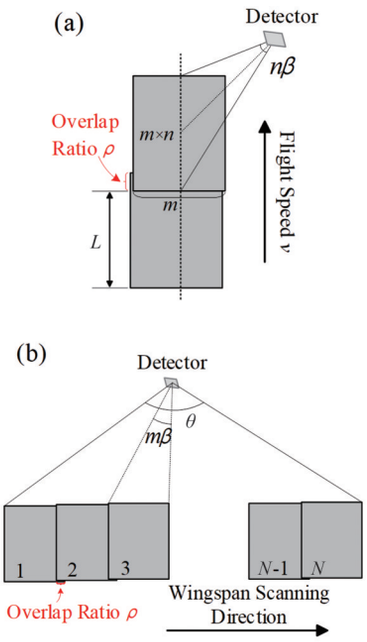

Fig. 2 Schematic diagram of FOV overlap: (a) FOV overlap in flight direction; (b) FOV overlap in wingspan direction
图2 视场重叠示意图:(a)飞行方向的视场重叠;(b)翼展方向的视场重叠

lows:

$$
\begin{aligned}
L &= Hn\beta(1-\rho)\\
t &= \frac{L}{v} = n\beta(1-\rho)\frac{H}{v}\\
t_{\text{eff}} &= \eta t = \eta n\beta(1-\rho)\frac{H}{v}\\
\omega &= \frac{\theta}{t_{\text{eff}}} = \frac{\theta}{\eta n\beta(1-\rho)} \times \frac{v}{H} = c_1\frac{v}{H}\\
c_1 &= \frac{\theta}{\eta n\beta(1-\rho)}
\end{aligned}
\quad . \quad (1)
$$

1.2 Basic constant-speed scanning strategy

1.2.1 Single-pass constant-speed scanning

The CA261 series camera, manufactured by Raytheon, uses an area-array detector for single-pass constant-speed scanning [2]. This camera is used for reconnaissance flights under medium to low speed height ratio conditions. After each pass of constant-speed scanning, a rapid return sweep is needed to reset the system to the initial position, followed by acceleration to the scanning speed for the next pass.

The scanning time for each pass is t, and the relationship between scanning speed and time is shown in Fig. 3(a). The green area in the figure represents the total FOV angle θ. The acceleration time from the initial position is t_1, the constant-speed scanning time is t_ω, and the acceleration during the reversal is a.

The parameter relationships for single-pass constant-speed scanning are shown in Fig. 3(b). When the angular velocity $\omega=3\theta/t$, the minimum acceleration is $a_{\min}=27\theta/t^2$, and the scanning efficiency is $\eta_{\text{single}}=33\%$. The method requires a large acceleration and has low scanning efficiency.

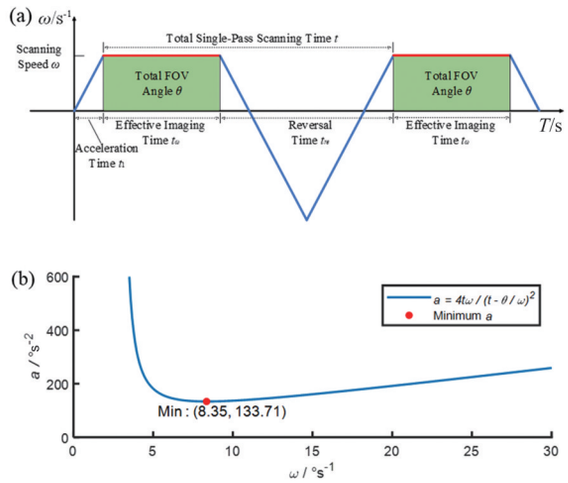

Fig. 3 Diagram of parameter relationships for single-pass constant-speed scanning: (a) speed-time schematic diagram; (b) acceleration-speed relationship curve
图3 单程匀速扫描参数关系图:(a)速度-时间示意图;(b)加速度-速度关系曲线

1.2.2 Double-pass constant-speed whisk-broom scanning

The area-array infrared camera, independently developed by Shanghai Institute of Technical Physics, employs a double-pass constant-speed scanning scheme [13]. Compared to single-pass constant-speed scanning, this approach eliminates the need for a rapid return sweep. In the wingspan scanning direction, only a velocity reversal is required to initiate the reverse scan, allowing the camera to capture two wide-field images in one whisk-broom cycle.

The relationship between scanning speed and time is shown in Fig. 4(a). The green area in the figure represents the total FOV angle θ.

The relationship between acceleration and scanning

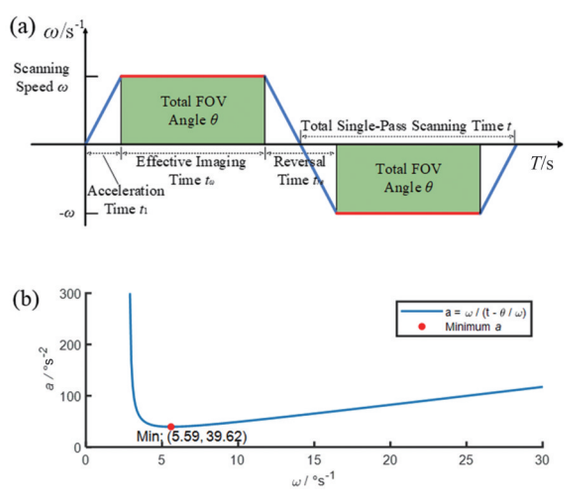

Fig. 4 Diagram of parameter relationships for double-pass constant-speed scanning: (a) speed-time schematic diagram; (b) acceleration-speed relationship curve
图4 双程匀速扫描参数关系图:(a)速度-时间示意图;(b)加速度-速度关系曲线

speed is shown in Fig. 4(b). When the angular velocity is $\omega=2\theta/t$, the minimum acceleration is $a_{\min}=8\theta/t^2$, and the scanning efficiency is $\eta_{\text{double}}=50\%$. When the acceleration is $a=49\theta/5t^2$, the scanning efficiency increases to $\eta'_{\text{double}}=71.4\%$.

For the entire whisk-broom system, further increasing the speed-to-height ratio will proportionally reduce the scanning time for each pass. The motor needs to provide a torque output that increases quadratically, complicating motor control and reducing scanning efficiency. Therefore, it remains necessary to optimize the scanning strategy.

2 Variable-speed whisk-broom strategy and vertical flight path LOS correction

2.1 Sinusoidal variable-speed whisk-broom strategy

In response to the current system limitations, we propose a sinusoidal double-pass variable-speed roll scanning strategy. The scanning position follows a cosine curve, resulting in a sinusoidal speed curve. This eliminates abrupt changes in speed and acceleration, reduces the system's torque output requirements during scanning, and enhances scanning efficiency. The relationship between scanning speed and time is illustrated in Fig. 5.

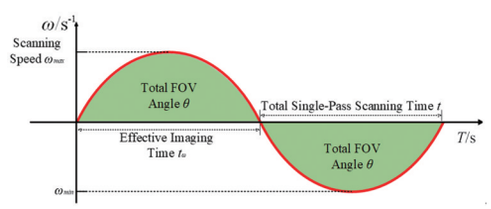

Fig. 5 Speed-time schematic diagram for double-pass variable-speed scanning
图5 双程变速扫描速度-时间示意图

The scanning motion relationships are as follows:

$$\begin{aligned}\theta_{\text{roll}} &= \frac{\theta}{2}\sin\left(c_2\frac{v}{H}t\right)\\ \omega_{\text{roll}} &= \frac{\theta}{2}c_2\frac{v}{H}\cos\left(c_2\frac{v}{H}t\right)\\ a_{\text{roll}} &= \frac{\mathrm{d}\omega}{\mathrm{d}t} = \frac{\pi^2}{2}\frac{\theta}{t^2}\sin\left(c_2\frac{v}{H}t\right)\\ c_2 &= \frac{\pi}{n\beta(1-\rho)}\end{aligned}, \tag{2}$$

where θ_{roll} is the position curve, ω_{roll} is the speed curve, and c_2 is a constant.

This variable-speed whisk-broom scheme utilizes the entire scanning process for imaging, maximizing the scanning time for each pass. Considering the reset time of the forward motion mechanism, the system efficiency can reach up to 90%, representing a further improvement over the double-pass constant-speed scanning scheme. The maximum acceleration amplitude is $a_{\max}=\pi^2\theta/2t$, reducing the peak acceleration by 50% and the average acceleration by approximately 70%, thereby decreasing the torque demand on the motor during reversals. This approach offers an effective solution for roll-scanning cameras under high speed-to-height ratio conditions and shows great potential for practical applications.

Compared to trapezoidal wave control, sinusoidal wave-driven current is smoother, consisting primarily of fundamental wave currents without high-frequency harmonic components. This reduces fundamental wave copper loss by 38.2% and minimizes hysteresis losses. As a result, total power consumption decreases by approximately 60%, effectively addressing motor heating limitations.

2.2 Combined vertical flight path and LOS correction model

Double-pass whisk-broom scanning requires coordination between forward image motion compensation in the flight direction and vertical flight path correction in the wingspan direction. Without this, adjacent images will have no overlapping areas, resulting in a step-like overall image, which hinders subsequent stitching, as shown in Fig. 6. Trajectory deviation can be divided into forward image motion deviation in the flight direction and scanning trajectory deviation in the wingspan direction.

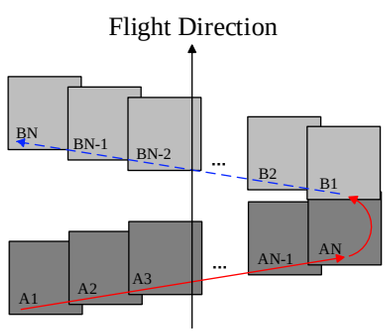

Fig. 6 Imaging schematic diagram without image motion compensation in the flight direction
图6 无飞行方向像移校正的成像示意图

2.2.1 Image motion in the flight direction

The generation and compensation principle of trajectory deviation in the flight direction is illustrated in Fig. 7. The rectangular box represents a simplified system, where the pitch mirror can rotate around the pitch axis to redirect the optical path for ground imaging. When the aircraft is directly above the ground point, the pitch mirror tilts at an angle of 45°. As the aircraft moves forward, the pitch mirror rotates in the opposite direction to maintain the LOS stable at the nadir point.

2.2.2 Scanning deviation in the wingspan direction

The scanning trajectory deviation in the wingspan direction is shown in Fig. 8. When the system performs whisk-broom motion under a large FOV, the actual ground projection of the LOS varies significantly relative to the flight altitude. In the traditional scheme [4], forward image motion compensation results in the LOS landing on a conical surface with a radius equal to the flight altitude H. When the forward tilt angle is small, the

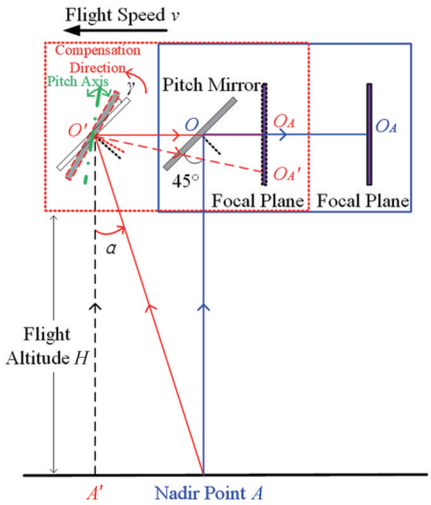

Fig. 7　Principle diagram of image motion compensation in the flight direction
图 7　飞行方向像移校正原理图

ground projection of the LOS is near the horizontal line. However, as the forward tilt angle increases, the ground projection deviates significantly from the vertical flight path, and the deviation intensifies as the scan angle increases. The solid line in the figure represents the hyperbolic trajectory of the scanning path, indicating the need for a revised compensation strategy.

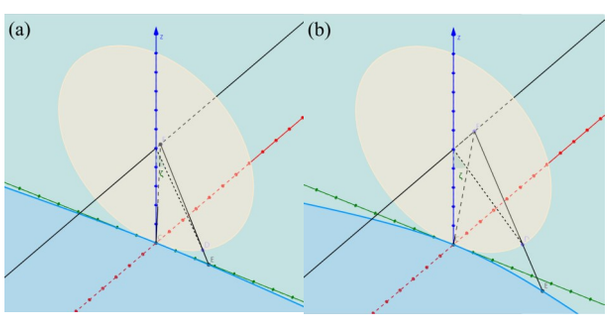

Fig. 8　Schematic diagram of track deviation in wingspan direction scanning: (a) small forward tilt angle condition; (b) large forward tilt angle condition
图 8　翼展方向扫描航迹偏差示意图:(a)小前向倾角条件;(b)大前向倾角条件

2.2.3　Design of the combined LOS path correction

Considering the half-cycle motion, the scanning system begins its wingspan direction sweep from the aircraft directly above point A and scans half of the total FOV angle along the vertical flight path, reaching the maximum FOV angle A' on one side. The relationship between the scanning angle $\Phi(t)$ and time is given by Eq. (2). In the flight direction, the system moves forward at speed v, traveling from the starting point O to O' over time t. The aircraft's flight altitude is H, and the pitch mirror rotates around the pitch axis to perform corrective compensation, stabilizing the LOS along the x-axis of the vertical flight path. From the FOV angle Φ, the actual height H' from the camera to the scanning point can be calculated, which in turn provides the actual LOS deviation angle α.

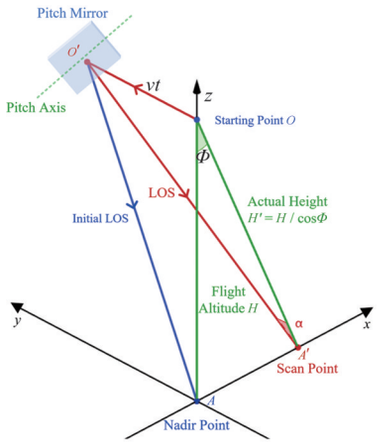

Fig. 9　Principle diagram of combined vertical track correction
图 9　联合垂直航迹校正原理图

The expressions for the scanning angle Φ, actual height H', and LOS deviation angle α are as follows:

$$\begin{aligned}\Phi(t) &= \frac{\theta}{2}\sin\left(c_2\frac{v}{H}t\right)\\ H(t)' &= \frac{H}{\cos\Phi(t)}\\ \alpha(t) &= \arctan\left(\frac{vt}{H(t)'}\right) = \arctan\left(\frac{v}{H}\cos\Phi(t)\right)\\ &= \arctan\left\{\frac{v}{H}t\cos\left[\frac{\theta}{2}\sin\left(c_2\frac{v}{H}t\right)\right]\right\}\end{aligned} \quad (3)$$

According to the principle of optical reversibility, during the scanning cycle, controlling the pitch mirror to perform a reverse compensation of $\alpha/2$ around the pitch axis can stabilize the LOS along the vertical flight path for scanning motion.

The expressions for the pitch compensation angle γ and compensation speed are as follows:

$$\begin{aligned}\gamma(t) &= \frac{1}{2}\alpha(t) = \frac{1}{2}\arctan\left\{\frac{v}{H}t\cos\left[\frac{\theta}{2}\sin\left(c_2\frac{v}{H}t\right)\right]\right\}\\ \omega_{\text{pitch}}(t) &= \frac{\mathrm{d}\gamma(t)}{\mathrm{d}t} = \frac{1}{1+\left\{\frac{v}{H}t\cos\left[\frac{\theta}{2}\sin\left(c_2\frac{v}{H}t\right)\right]\right\}^2}\cdot\\ &\quad\left\{\frac{v}{H}\cos\left[\frac{\theta}{2}\sin\left(c_2\frac{v}{H}t\right)\right]-\right.\\ &\quad\left.c_2\left(\frac{v}{H}\right)^2 t\sin\left[\frac{\theta}{2}\sin\left(c_2\frac{v}{H}t\right)\right]\frac{\theta}{2}\cos\left(c_2\frac{v}{H}t\right)\right\}\end{aligned} \quad (4)$$

According to Eq. (4), the position and speed functions of the pitch compensation mirror involve nested trigonometric functions, leading to high computational complexity and significant hardware resource consumption.

In hardware implementations, both the position loop and speed loop require complex trigonometric calculations, consuming considerable hardware resources and hinder real-time compensation. Therefore, simplification and approximation are needed to reduce the complexity of the control algorithm and achieve efficient compensation.

By performing a polynomial expansion and approximation optimization on the trigonometric functions such as arctan in the LOS deviation angle α, and ignoring higher-order terms beyond the seventh order, the following equation is obtained:

$$\alpha(t)=\frac{v}{H}t-\frac{1}{8}\theta^2{c_2}^2\left(\frac{v}{H}\right)^3t^3+\frac{1}{24}\theta^2{c_2}^4\left(\frac{v}{H}\right)^5t^5-\frac{1}{602}\theta^4{c_2}^6\left(\frac{v}{H}\right)^7t^7+O(t^9)$$

$$\omega_{\text{pitch}}(t)=\frac{1}{2}\frac{\mathrm{d}\alpha(t)}{\mathrm{d}t}=\frac{v}{H}-\frac{3}{8}\theta^2{c_2}^2\left(\frac{v}{H}\right)^3t^2+\frac{5}{24}\theta^2{c_2}^4\left(\frac{v}{H}\right)^5t^4-\frac{1}{86}\theta^4{c_2}^6\left(\frac{v}{H}\right)^7t^6+O(t^8) \quad (5)$$

Considering only the approximation error in the compensation algorithm, the optimized compensation function yields a LOS correction deviation of less than 0.5% at a maximum scanning angle of 40°, and less than 0.8% globally, achieving precise vertical flight path correction. Compared to the nested trigonometric function approach for exact calculations, this scheme simplifies the process using a polynomial expansion, significantly reducing the control complexity in both the position loop and speed loop of the control system, thereby improving the system's real-time performance.

3 Experimental verification and discussions

A half-cycle simulation was conducted to verify the accuracy of the correction path algorithm. The correction algorithm path, compared to the theoretical position curve, is presented in Fig. 13(a), while the deviation curve is shown in Fig. 13(b). The correction algorithm's compensation deviation was on the order of 10^{-4} compared to the theoretical curve. Under an instantaneous FOV of 250 μrad, the overall deviation was better than 1.8 pixels. During a single frame exposure time of 10 ms, the maximum deviation angle was 9.8×10^{-5} rad, which was better than 0.4 pixels, meeting the requirements for LOS compensation.

On the hardware platform, a single-step simulation was used to compare the optimized LOS path algorithm proposed in this study with the CORDIC algorithm. The time difference between the end of the calculation and the reset point defined the single-step computation time. At t = 0.15 s, the theoretical LOS position was 0.031 29 rad, while the calculated value from the proposed LOS correction algorithm was 0.031 25 rad, with a deviation of 40 μrad and a computation time of 75 ns. In comparison, the CORDIC algorithm calculated the position as

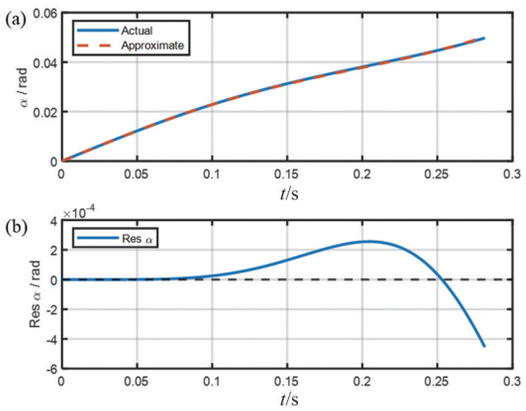

Fig. 10 Correction algorithm curve and theoretical position curve: (a) angle curve; (b) residual curve
图10 校正算法曲线与理论位置曲线:(a)角度曲线;(b)偏差曲线

0.031 37 rad, with a deviation of 80 μrad and a computation time of 645 ns. The proposed method reduced the computation time by an order of magnitude, benefiting real-time compensation.

The LOS correction effect and the fitted curve at different time points are shown in Fig. 11. The fitted curve aligned well with the simulation curve, with an error ranging from -0.4 mrad to 0.4 mrad. The computation time per step was consistently 75 ns, enabling LOS correction and compensation for the vertical flight path.

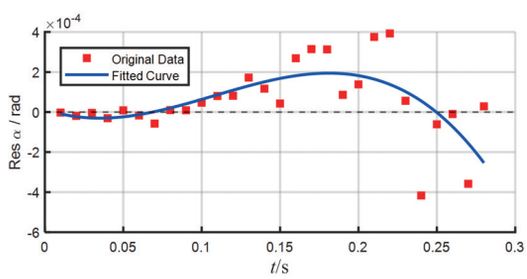

Fig. 11 Correction effect of LOS
图11 视轴校正效果

A long-focus pod camera with a single-frame FOV of 9.33°×9.33° was used as the experimental subject. A visible light area-array camera with the same technical specifications was used to replace the area-array infrared camera for functional verification. The camera achieved 70° wide-field coverage through seven exposures. The equipment was mounted on a simulated flight test platform for imaging experiments, using the aircraft's actual attitude variation curve within a single flight strip as input, as shown in Fig. 12. The pointing commands were superimposed and compensated for using attitude information feedback from the POS.

The comparison of imaging results for the forward-pass and return-pass scans are shown in Figs. 13 and 14. The dashed rectangular box represents the FOV for a single image, with the center of the rectangle corresponding to the LOS center. The solid rectangular box indi-

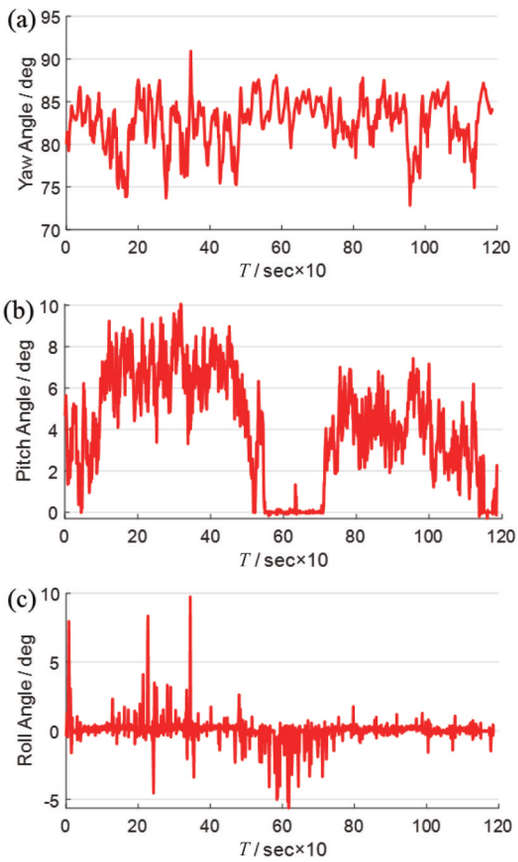

Fig. 12 Aircraft attitude angle change curves: (a) yaw; (b) pitch; (c) roll
图 12 载机姿态角度变化曲线:(a)方位角;(b)俯仰角;(c)横滚角

cates the stitching alignment area, which remains consistent for both methods. In the traditional method, the maximum LOS deviation between the first and last frames of each scan was 29 pixels, corresponding to 0.39°. In contrast, the new method proposed in this study reduced the maximum deviation to 5 pixels, corresponding to 0.07°. The central LOS remained essentially aligned with the horizontal line of the vertical flight path, confirming the effectiveness of the vertical flight path LOS correction method proposed in this study.

The LOS pointing deviations for the two scanning methods illustrated above are shown in Table 1, where (a)-(g) correspond to the exposure sequence of the seven images. The center of the FOV for the center exposure image (d) was selected as the horizontal LOS reference point for each row of images. With this method, the root mean square (RMS) of the central LOS stability deviation was improved from 9.23 pixels, as seen in the traditional method, to 2.78 pixels.

From the data in Table 1, it is observed that using the new vertical flight path correction method, the exposure images near the center point of each image row show pixel errors relative to the horizontal axis ranging from 1 pixel to 2 pixels, corresponding to 0.25 - 0.5 mrad. For exposure images located at the boundary of a single row (roll angle $\Phi = 30^\circ$), the vertical deviation relative to the central horizontal axis is approximately 4 pixels, corresponding to 1 mrad. In the previously discussed simulation of the optimized algorithm, the error near the central exposure point is approximately 0.2 mrad, while the error near the boundary of a single row is 0.4 mrad. The comparison indicates that during the simulated flight imaging experiments, a system error of approximately 0.6 mrad still exists.

The traditional algorithm did not account for changes in actual imaging elevation caused by roll rotation. Compared with the new vertical flight path algorithm, the pitch angle of the camera in the traditional algorithm differed by a factor of the cosine of the roll angle. As a result, the imaging position gradually deviated from the horizontal flight path as the roll angle increased, with cumulative errors observed. This trend aligns with the incremental pixel error shown in Table 1. Considering the exposure position at the boundary of a single row with a roll angle of $\Phi = 30^\circ$, the pitch compensation angle for the new algorithm was $\alpha_1 = 0.04$ rad. In contrast, for the traditional algorithm, after applying a slow factor of $n = 0.93$, the pitch compensation angle was calculated as $\alpha_2 = \alpha_1 / (n\cos\Phi) = 0.043$ rad. The compensation deviation in this case was 3 mrad, corresponding to 12 pixels.

Fig. 13 Comparison of imaging effects during forward-pass scanning: (a) traditional method; (b) new method
图 13 去程扫描成像效果对比:(a)传统方法;(b)新方法

Fig. 14 Comparison of imaging effects during return-pass scanning: (a) traditional method; (b) new method
图14 回程扫描成像效果对比:(a)传统方法;(b)新方法

Table 1 LOS stability deviation in area-array imaging systems
表1 面阵成像系统视轴稳定偏差

Method		Deviation (px)							RMS
		(a)	(b)	(c)	(d)	(e)	(f)	(g)	
Traditional	forward-pass	−14	−9	−2	0	3	9	15	9.23
	return-pass	14	10	2	0	−3	−8	−14	9.02
New	forward-pass	−2	0	−2	0	−1	−2	−5	2.33
	return-pass	4	2	1	0	1	4	4	2.78

Comparing this result with the data in Table 1, a system error of 2 pixels, equivalent to 0.5 mrad, was observed.

In the experimental model used in this study, system errors were classified into random errors, measurement errors, control errors, and stitching errors. Since the POS attitude was a known input under experimental conditions, the random error was attributed to the synchronization attitude error of the attitude simulation platform. The measurement error originated from the encoder feedback error, with the encoder system employing a 26-bit absolute encoder that achieved an accuracy of 0.058 mrad. Control error referred to the pointing error of the servo motor, which could result in certain delay errors due to the computation cycle and servo delay. As the primary objective of this experiment was to verify the control path planning of the LOS center point, no post-processing was applied to the images, and only simple stitching was performed. Due to edge field distortion in area-array imaging, a stitching error was also present, which was calculated as 1 pixel, equivalent to 0.25 mrad. In summary, the servo control mechanism introduced approximately 0.2 mrad of control error. This could be further improved in future studies to enhance the pointing accuracy of the LOS.

The 70° wide-field imaging effect based on vertical flight path LOS compensation is shown in Fig. 15. The system delivered good imaging performance, with rich image information and clearly discernible target details. Due to the simple stitching applied to the images, some geometric distortions were observed in the buildings, but the central FOV exhibited good overlap.

As with the majority of studies, the current study was subject to limitations. The combined correction LOS path design proposed in this study was based on the assumption that all imaging rows were at the same ground elevation. This strategy was less applicable to steep mountainous terrains with significant ground elevation variations. If the ground elevation changed significantly within an imaging row, a corresponding scanning strategy would need to be designed based on the actual terrain.

Fig. 15 Wide-field imaging based on vertical flight path LOS compensation
图15 基于垂直航迹视轴补偿的宽视场成像效果

4 Conclusions

To address the efficiency limitations of current wide-field, high-resolution imaging systems during high-speed reversals, this study proposes a novel sinusoidal variable-speed whisk-broom scanning scheme. This method utilizes the entire scanning time for imaging, improving time efficiency by approximately 18.6% compared to constant-speed whisk-broom scanning. To solve the problem of forward constant-speed image motion compensation being unsuitable for large forward tilt angles and large scanning FOV angles, a forward image motion compensation strategy based on vertical flight path correction is proposed. The compensation curve calculation is optimized to enhance computational efficiency, achieving a LOS compensation accuracy better than 0.4 mrad. Using an area-array camera on a simulated flight test platform, an external imaging experiment was conducted to verify the feasibility of the variable-speed scanning method and vertical flight path LOS correction. The experiment produced wide-field, high-resolution images with a stable horizontal LOS. This research is of great significance for advancing airborne whisk-broom imaging technology towards wider fields of view, higher speed-to-height ratios, and higher resolutions.

References

[1] Wang C R, Yang L F, Cao X, et al. Recent progress of airborne infrared remote sensing technology in SITP [J]. J. Infrared Millim. Waves, 2022, 41(1): 110-121.
王崇儒,杨利峰,曹汛,等. 航空红外光电遥感技术最新进展[J]. 红外与毫米波学报, 2022, 41(1): 110-121.
[2] Lareau A G. Flight demonstration of the CA-261 step frame camera [C]. Proceedings Volume 3128, Airborne Reconnaissance XXI. Optical Science, Engineering and Instrumentation '97, 1997, San Diego, CA, United States: SPIE, 1997: 17-28.
[3] Pang Y, Liang X J, Jia W, et al. The comprehensive airborne remote sensing experiment in saihanba forest farm [J]. National Remote Sensing Bulletin, 2021, 25(4): 14.
[4] Iyengar M, Lange D. The Goodrich 3rd generation DB-110 system: operational on tactical and unmanned aircraft [C]. Proceedings Volume 6209, Airborne Intelligence, Surveillance, Reconnaissance (ISR) Systems and Applications III. Defense and Security Symposium, 2006, Orlando (Kissimmee), Florida, United States: SPIE, 2006: 620909.
[5] Wang C R, Han G C, Jin X B, et al. A new method for LOS path planning and overlap rate setting of airborne area-array whisk-broom imaging[J]. J. Infrared Millim. Waves, 2023, 42(3): 383-390.
王崇儒,韩贵丞,金祥博,等. 一种机载面阵摆扫成像视轴路径规划与重叠率计算的新方法[J]. 红外与毫米波学报, 2023, 42(3): 383-390.
[6] Li S, Hu Y, Gong C L, et al. A step-by-step geometric correction and error analysis of swing-swept array thermal infrared aerial image [J]. J. Infrared Millim. Waves, 2020, 39(2): 242-250.
李赛,胡勇,巩彩兰,等. 面阵摆扫热红外航空影像分步几何校正方法[J]. 红外与毫米波学报, 2020, 39(2): 242-250.
[7] Qiao C, Ding Y L, Xu Y S, et al. Ground target geo-location using imaging aerial camera with large inclined angle[J]. Optics and Precision Engineering, 2017, 25(07): 1714-1726.
[8] Du Y L, Ding Y L, Xu Y S, et al. Geo-location algorithm for TDI-CCD aerial panoramic camera [J]. Acta Optica Sinica, 2017, 37(3): 355-365.
[9] Wang Y K, Han G C, Qi H X, et al. Investigation of image motion compensation technique based on real-time LOS tracking[J]. J. Infrared Millim. Waves, 2015, 34(6): 757-762.
王义坤,韩贵丞,亓洪兴,等. 基于实时视轴跟踪的像移补偿技术研究[J]. 红外与毫米波学报, 2015, 34(6): 757-762.
[10] Hong S Y, Wang Y K, Han G C, et al. Study on real-time LOS stabilization technique based on dual reflectors in the airborne remote sensing imaging system[J]. Aero Weaponry, 2020, 27(5): 86-90.
[11] Liu Y B, Wang Y K, Han G C, et al. Aviation wide field thermal imaging technology based on array detector sweep-stop pattern [J]. J. Infrared Millim. Waves, 2017, 36(3): 330-335.
刘毓博,王义坤,韩贵丞,等. 基于摆停模式的航空大视场面阵热成像技术[J]. 红外与毫米波学报, 2017, 36(3): 330-335.
[12] Jiang B, Ge M F, Liu M, et al. Research on image stabilization technology of area-array aerial camera[J]. Infrared and Laser Engineering, 2014, 43(10): 3467-3473.
[13] Wang Y K, Qi H X, Han G C, et al. Study on light-small whisk-broom scanning thermal imaging system with area-array detector[J]. Laser & Infrared, 2017, 36(3): 330-335.